CrossMark

Preliminary assessment of the ATHENA/WFI non-X-ray background

Emanuele Perinati[1] · Marco Barbera[2,3] ·
Sebastian Diebold[1] · Alejandro Guzman[1] ·
Andrea Santangelo[1] · Chris Tenzer[1]

Abstract We present a preliminary assessment of the non-X-ray background for the WFI on board ATHENA conducted at IAAT in the context of the collaborative background and radiation damage working group activities. Our main result is that in the baseline configuration originally assumed for the camera the requirement on the level of non-X-ray background could not be met. In light of the results of Geant4 simulations we propose and discuss a possible optimization of the camera design and pinpoint some open issues to be addressed in the next phase of investigation. One of these concerns the possible contribution to the non-X-ray background from soft protons and ions funneled to the focal plane through the optics. This is not quantified at this stage, here we just briefly report on our ongoing activities aimed at validating the mechanisms of proton scattering at grazing incidence.

1 Introduction

The *Wide Field Imager* (WFI) [1] is one of the two focal plane instruments proposed for ESA's *Advanced Telescope for High Energy Astrophysics* (ATHENA) [2]. It consists of a Si-based detector developed at the Max-Planck-Institut für extraterrestrische Physik (MPE), structured in two parts (Fig. 1): a large chip with 40′

✉ Emanuele Perinati
emanuele.perinati@uni-tuebingen.de

1 IAAT - Institut für Astronomie und Astrophysik, Universität Tübingen, 72076 Tübingen, Germany

2 DFC - Dipartimento di Fisica e Chimica, Università di Palermo, 90123 Palermo, Italy

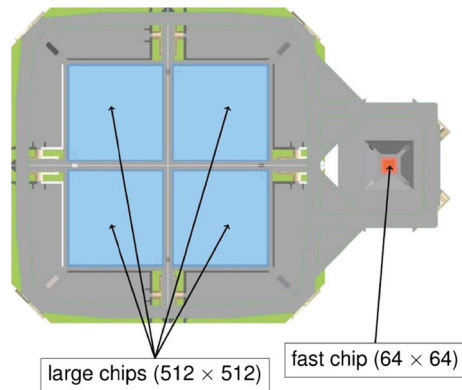3 INAF - Osservatorio Astronomico di Palermo, 90134 Palermo, Italy

Fig. 1 The proposed ATHENA/WFI instrument features a large detector divided into four quadrants (512 × 512 pixel each) mounted in the focus of the telescope plus a small (64 × 64 pixel) fast detector mounted defocused by 35 mm. (image credits: MPE)

× 40′ FOV mounted in the focus of the telescope, divided into four quadrants of 512 × 512 pixel each; and a small 64 × 64 pixel fast chip mounted defocused by 35 mm, for the observation of bright sources.

Each pixel is a DEPFET, i.e. an active sensor consisting of a low capacitance p-channel MOSFET implanted on a high resistivity sideward depleted n-type Si substrate, allowing for in-situ amplification of the charge generated by the absorbed X-rays, which results in a rapid low noise readout without charge transfer. The WFI will provide sensitive wide field imaging in the range 0.1–15 keV, with moderate spectral resolution (< 150 eV @6 keV), high time resolution (~ 1.3 msec for the large chip and ~80 μsec for the small chip, in full frame mode) and high count-rate capacity (~ 1 Crab), complementing the exquisite spectral capabilities of the X-ray Integral Field Unit (X-IFU) [3]. In this article we present an overview of the WFI non-X-ray background based on studies currently in progress at our institute, one of the WFI Consortium members collaborating with the MPE in the effort of predicting the diverse components of the instrumental background and optimizing the camera design to improve the performance of the detector as well as the strategies for the monitoring and the rejection of the background in-flight.

2 Non-X-ray background

The level of instrumental background limits the sensitivity achievable by the WFI and it is one of the aspects driving the design of the camera. At lower energies (< 2 keV) the instrumental background is expected to be dominated by diffuse X-rays of galactic and extragalactic (the so-called Cosmic X-ray Background (CXB) emission) origin focussed by the optics. On the other hand, at higher energies the dominant contribution is expected from Galactic Cosmic Rays (GCRs), i.e. omnidirectional energetic charged particles, mostly protons, present in the space environment. Softer protons and ions possibly funneled to the focal plane through the optics may also contribute to lower the sensitivity (see Section 4). The particle background is usually referred to as non-X-ray background (NXB). An overall NXB count-rate ~ $5 \cdot 10^{-3}$ cts/cm^2/s/keV has been

adopted as a scientific performance requirement for both the WFI and the XIFU, a value quite similar to the close-pos continuum NXB measured by the pnCCD on board XMM, orbiting in an environment where the fluxes of GCRs are expected not too different from those in L2 [4], where ATHENA is planned to be operated. Considering the much larger effective area of ATHENA compared to XMM, an XMM-like NXB would still guarantee a significant improvement in sensitivity. As the requirement is an upper limit, an NXB count-rate below that value would be a goal and efforts are being made to optimize the configuration and the rejection algorithms, in order to minimize the expected rate of false counts generated by environmental radiation. The residual NXB will be mostly due to secondary particles originating from structural components of the mass distribution at the focal plane, as false counts produced by the direct interaction of primary GCRs with the detector can be rejected with very high efficiency (> 99.5%). This is because the depleted volume is relatively thick (450 μm) and, by geometry, in most cases impinging protons will travel in it paths longer than 40 μm. As the minimum of ionization by protons in Si is ~ 0.4 keV/μm (Fig. 2), most of the protons will deposit in the depleted volume an amount of energy >15 keV. Protons impinging at angles sufficiently small may be able to deposit <15 keV only in pixels belonging to the very peripheral part of the detector, where the profile of the point spread function gets flattened, hence these events will actually have a minor impact on the observations.

The current WFI baseline configuration envisages a 4 cm thick Al shield in order to prevent protons up to ~110 MeV from reaching the detector. Although these protons constitute only a small fraction of the overall environmental flux, they are the most harmful having a higher non-ionizing energy loss (NIEL) in Si (Fig. 3), that can lead to the generation of defects in the crystal by atomic displacement. On the other hand, the shield itself acts as a source of NXB, generating showers of secondary particles, to a larger extent electrons and X-rays, when energetic protons strike it. Softer electrons
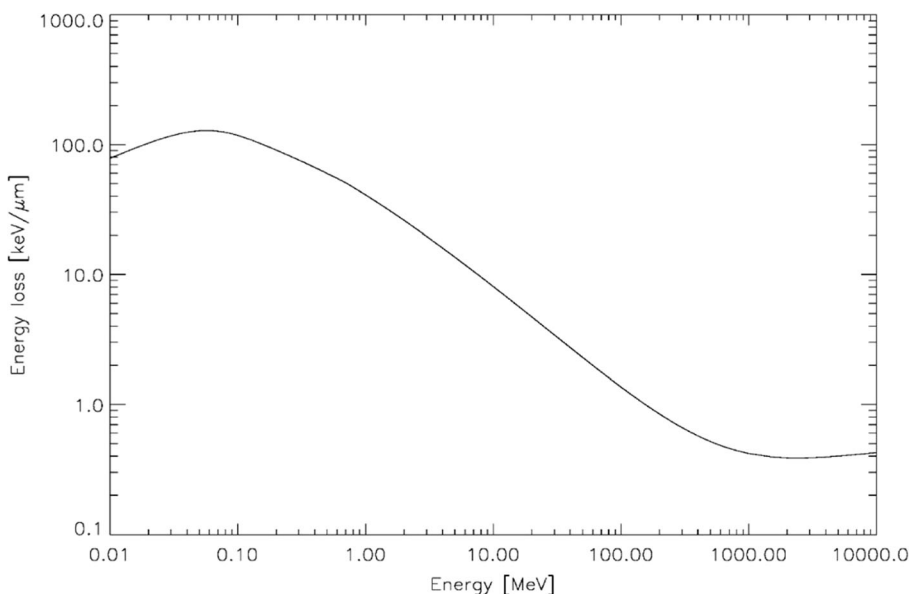

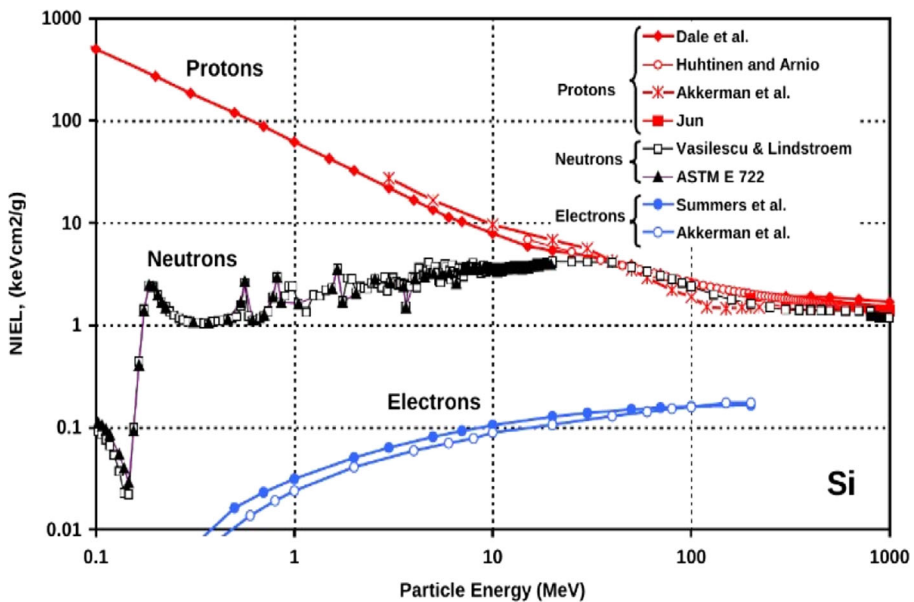Fig. 2 Average energy loss of protons in Si (from NIST online dataset)

Fig. 3 NIEL of protons, electrons and neutrons in Si as a function of their energy (image credits: C. Poivey)

ejected from the front surface of the shield with an energy in the detector band give valid absorption patterns that cannot be discriminated by those of signal X-rays. Higher energy electrons can also contribute to the NXB if they undergo backscattering at the detector surface, penetrating into the sensitive volume only over a small distance before being reflected, thus depositing just a small fraction of their energy which may fall in the detector band. Softer X-rays generated inside the shield by Bremsstrahlung can escape onto the detector, clearly they also give absorption patterns that cannot be distinguished from those of signal X-rays. Harder X-rays with energy >15 keV can generate false counts by Compton scattering in the Si crystal. Primary energetic protons can excite fluorescence as well, resulting in the emission of X-rays at characteristic energies producing spectral features in the NXB spectrum. In the case of a shield in Al a line at ~1.5 keV is expected. Furthermore, energetic protons may generate secondary neutrons by nuclear spallation in the shield, which may contribute to increase both the NXB, via elastic scattering in Si, and the NIEL (Fig. 3).

3 Geant4 simulations

3.1 Basic camera head

In this section we report results of simulations done in Geant4 10.01.p02 using the basic camera head configuration, i.e. the shield plus the detector floating inside (sub-structures, e.g. baffle, filter-wheel, etc., are not included at this stage), as shown in Fig. 4. The shield is modelled as a 4 cm thick Al box. The analysis is restricted to the large chip (for the small chip the NXB is not an issue, as it is intended for bright sources), which is modelled as a Si slab of 15×15 cm^2 with 90 nm Al plating on top.
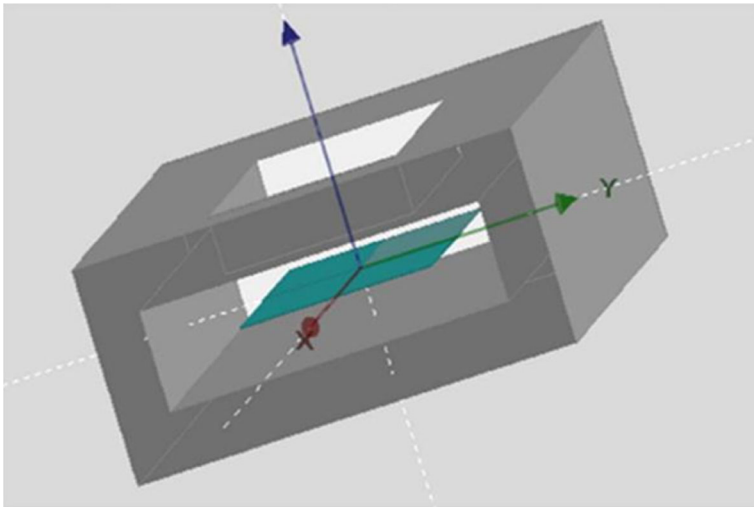
Fig. 4 The basic geometry used in these simulations: a 4 cm thick Al box with a Si slab floating inside (image credits:MPE)

Although it is a simplified description, it is sufficient for a first order estimate of the level of NXB to be expected on the detector, as this would be to a larger extent produced by the shield, while the sub-structures would contribute only to a lesser extent. Figure 5 shows the environmental fluxes we used as an input to simulations [5, 6]. Figure 5 also reports the response function of channel #11 of the SREM particle monitor onboard the Planck satellite [Buehler 2015, personal communication], which we used to validate the GC proton flux adopted for L2. In fact, the expected average cosmic proton flux F(E) (blue curve in Fig. 5) satisfies precisely the integral equation:

$$< C_{11} > = \int_{100}^{\infty} F(e)*R(E)dE$$

where $<C_{11}>$ is the average count-rate of channel #11 in the range of proton energies >100 MeV ($<C_{11}> \sim 0.45$ cts/s) and R(E) is the channel #11 response function (assumed constant above ~3 GeV [Buehler 2015, personal communication]). However, notice that the NXB levels reported hereunder have been obtained by normalizing the output of simulations to fluxes ~1.5 times larger than those shown in Fig. 5, in order to assume a more conservative case (which would correspond to solar minimum conditions instead of values averaged over the solar cycle).

3.1.1 NXB induced by GCRs

We simulated the residual NXB induced by the expected average fluxes of GCRs at L2. It consists mostly of secondary electrons (~ 50%) and X-rays (~ 45%), with a minor contribution (~ 3%) from elastic scattering in the Si lattice by spallation neutrons. Even smaller (~ 2%) is the number of false counts produced by the direct interaction of primaries with the detector, which in any case affect only border pixels, as previously explained. Due to the FOV aperture, the lower part of the shield contributes more NXB (~ 60%) than the upper part (~ 40%). The NXB slope slightly decreases with energy
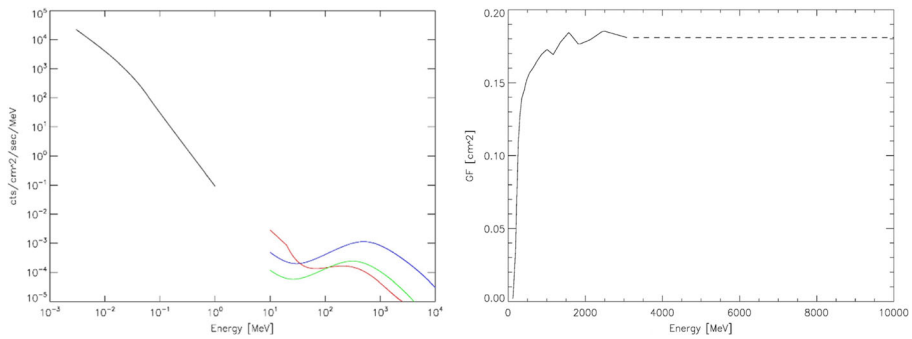
Fig. 5 *Left*: environmental fluxes used as an input to simulations: CXB photons (*black curve*), GC protons (*blue curve*), GC α-particles (*green curve*) and GC electrons (*red curve*). *Right:* response function (i.e. geometrical factor) of the channel #11 of the SREM aboard Planck

(Fig. 6) and at energies >7 keV the level is already close the required value. To reduce the NXB at energies <7 keV we investigated the application of a passivation layer on the non-illuminated side of the detector. The layer works primarily by cutting the softer electrons emitted from the lower part of the shield, which can be fully absorbed. To prevent electrons <15 keV from reaching the sensitive volume a few micron thick layer should be used, the specific thickness depends on the material. A technically feasible passivation may consist of 3 μm benzocyclobutene (C_8H_8). The blue curve in Fig. 6 shows the effect on the background. The layer does not add background as no gap is left in between, so that all secondaries generated in it can be rejected with the same efficiency as the primaries that excite them. Unavoidably, the layer introduces a shift in energy of the incoming electron flux, so that on one hand incoming electrons <15 keV get stopped, on the other hand incoming electrons >15 keV may undergo enough energy degradation traversing the layer to emerge with an energy in the WFI band. However, as the flux of secondary electrons ejected from the shield decreases with energy, as shown in Fig. 6, the resulting balance is positive, i.e. the NXB continuum effectively reduces by ~20% on average over the entire WFI band and by more than 30% at energies <7 keV, where the percentage of electrons in the NXB is higher. As a result, a nearly flat level ~ $6 \cdot 10^{-3}$ cts/cm^2/s/keV is achieved over the entire WFI band.
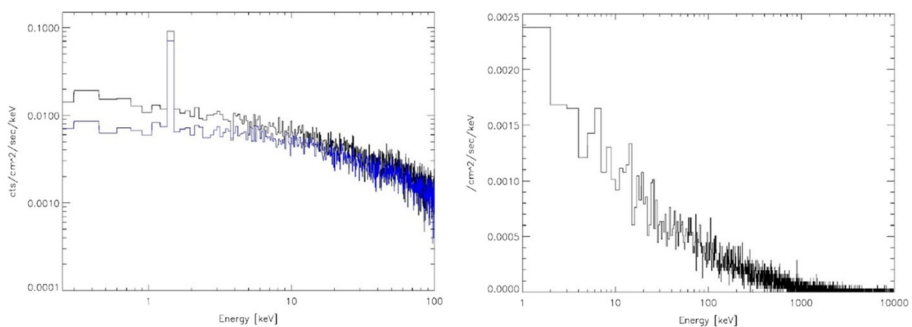

Fig. 6 *Left:* NXB induced by L2 GCRs in the basic camera head configuration. The *black curve* is the level corresponding to a WFI without passivation floating inside the Al shield. The *blue curve* is the level corresponding to a WFI with 3 μm C_8H_8 passivation on the non-illuminated side. *Right:* simulated flux of secondary electrons from the Al shield onto the WFI non-illuminated side

Notice that 90 nm Al and 3 μm C_8H_8 have both a transmissivity ~90% at ~1.5 keV, hence the NXB spectrum still contains a prominent fluorescence line originating from the Al shield. To get rid of this undesired feature, an internal low-Z layer in between the shield and the WFI can be used.

3.1.2 NXB induced by CXB

We simulated the residual NXB induced by the expected average CXB flux. Although lower energy CXB photons are fully absorbed in the Al shield, a fraction of higher energy (> 50 keV) photons can pass through it (e.g. 4 cm Al has ~16% transmissivity @ 100 keV) and reach the detector, where they interact with Si by Compton scattering (the scattering probability increases exponentially with thickness). Depending on the scattering angle, the amount of energy transferred to the recoiling electrons can fall in the detector band. This energy is then released from the recoiling electrons to the crystal by ionization and hence can contribute to the NXB. Figure 7 shows the simulated Compton spectrum on the detector.

3.1.3 NXB induced by GCRs + CXB

As shown is Fig. 8, combining the GCR NXB (Fig. 6) and the CXB NXB (Fig. 7) results in an overall NXB ~ 0.01 cts/cm^2/s/keV in the range < 15 keV, to a larger extent (~ 70%) composed by photons, while other particles (mostly electrons) contribute to the rest (~ 30%). This NXB level is about twice as large as the requirement. However, we stress that other mass distribution around the detector not included in the simplified geometry considered here (e.g. the optical bench, the X-IFU cryostat) would likely act as an additional equivalent shielding and may contribute to reduce to some extent the CXB contribution. On the other hand, such mass distribution may in turn become itself an additional source of secondary high energy photons. A FITS file containing the NXB dataset of Fig. 8 is available online at the WFI wikipage (https://wiki. mpe.mpg.de/ATHENA-WFI).
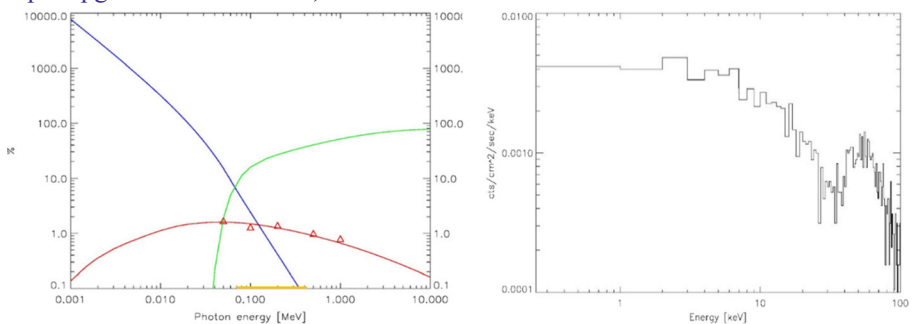

Fig. 7 *Left:* expected environmental CXB flux (*blue curve, units on the right y-axis*), photon transmissivity of 4 cm Al (*green curve*) and probability of Compton scattering in 450 μm Si (*red curve*) vs. energy. The triangles correspond to some data points simulated in Geant4 as a validation of the Compton scattering treatment. The range of CXB energies that do contribute to the NXB is marked in orange. *Right:* NXB generated by high energy CXB through Compton scattering in the WFI depleted volume. The peak around 50 keV is not due to Compton scattering, instead it comes from CXB photons fully absorbed in the depleted volume and reflects the behavior of the Al shield transmissivity and CXB vs. energy
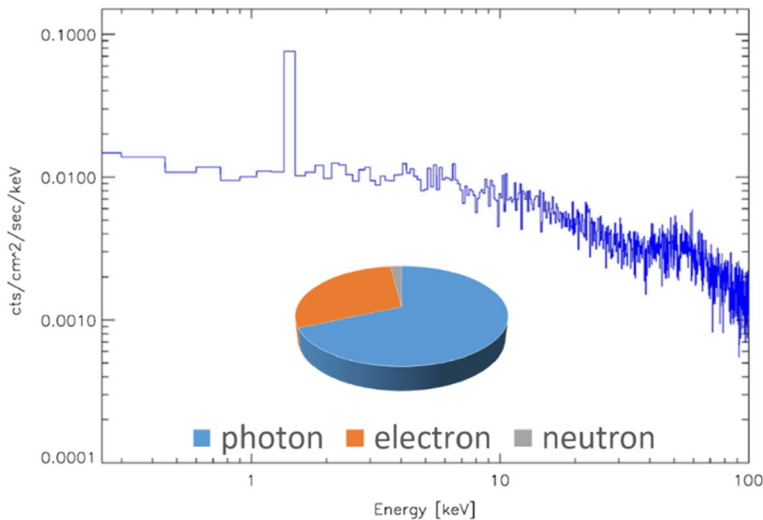
Fig. 8 Overall WFI NXB induced by GCRs and CXB. The pie-chart shows the relative weight of the different secondary particles in the simulated WFI NXB. Primary particles are not taken into account as their contribution to NXB is confined to border pixels

3.2 Multilayer internal shielding

We are currently investigating the trade off between NXB and NIEL in a number of possible improved shielding configurations. As a case study, we investigated a configuration which prefigures a 4 cm thick Al bulk shield plus an internal graded shield based on 2 mm Au (to fully suppress CXB leakage from the bulk) + 1 mm Al (to absorb the Au L-fluorescences) + 1 mm Be (to absorb the Al K-fluorescence and possibly reduce to some extent secondary soft electron emission towards the detector. Comparing in a simple test geometry consisting of closed spherical shells (Fig. 9) the NXB generated by GC protons in such multilayered configuration with the one generated by GC protons in a configuration based on a 4 cm Al shell only, the induced continuum NXB appears very similar in both cases and as desired the NXB spectrum corresponding to the multilayered configuration does not show any fluorescence (Fig. 9) in the detector band. As the NXB induced by the CXB is suppressed in the multilayered configuration, the latter would allow for a sensitivity improvement by a factor of ~2. However, due to the presence of Au the flux of spallation neutrons internally generated is ~3 times larger than that found in 4 cm Al only, in fact the yield of neutron generation by spallation is expected to increase linearly with the atomic mass of the material. The impact of such increased flux of neutrons in terms of additional NIEL has still to be evaluated. As another option, the Au layer could be applied as the outermost layer, the sequence could be in this case 2 mm Au + 4 cm Al + 1 mm Be (or B_4C or any other suited low-Z material). However, in such a configuration the surface of Au exposed to energetic protons would be significantly larger, which may result in an even higher flux of neutrons towards the detector.
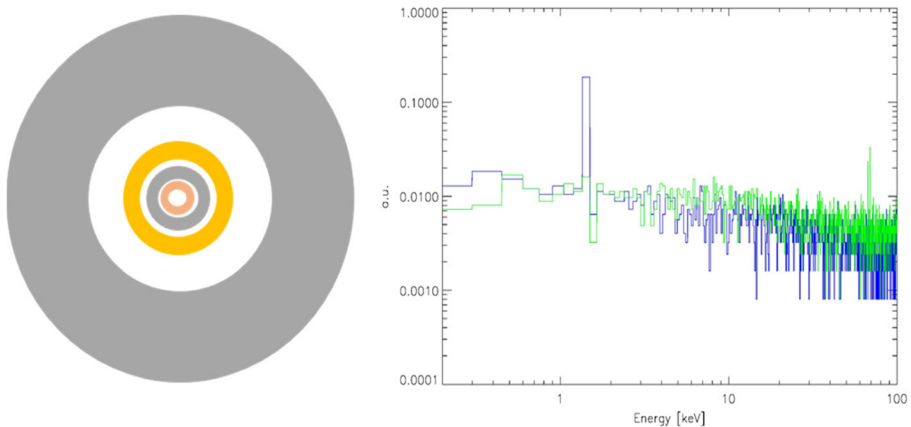
Fig. 9 A possible multilayered shielding consisting of 4 cm Al (grey) + 2 mm Au (yellow) + 1 mm Al (grey) +1 mm Be (pink). In this configuration the NXB induced from the CXB is suppressed (thanks to Au), while the NXB induced by GC protons (green curve) is about the same as in the case of a 4 cm Al shell only (blue curve). However, in this configuration a flux of spallation neutrons ~3 times larger is found. The units in the plot are arbitrary as the both NXB curves refer to the same closed spherical shell test geometry

3.3 Optical blocking filter

One of the sub-structures in the WFI camera configuration is the optical blocking filter (OBF) needed to reduce the load of visible/UV light to the detector. The current OBF baseline prefigures an external filter 30 nm Al + 150 nm Polyimide [7] coupled to a filter (90 nm Al) deposited onchip. The external filter will be positioned above the detector at a distance of several centimeters from it. Although the contribution to the NXB from the filter alone is most likely negligible, it is worth considering the overall effect of the filter and the mesh that is being investigated as a solution to mechanically sustain it. As a first case study, we investigated a squared mesh with the following specifications:

– size = 160 × 160 mm
– thickness = 0.25 mm
– width (i.e. wire transverse size) = 0.07 mm
– pitch (i.e. center-to-center distance between celles) = 3 mm

Three candidate materials have been initially considered: Al, Ti and stainless steel #316 (Fe 64%, Cr 18%, Ni 14%, Mo 2%, Mn 2%). We simulated the excess NXB that a mesh positioned above the WFI at 12 cm distance would generate on the detector. Figure 10 shows the resulting spectra. In all three cases, the excess continuum introduced by the mesh is negligible (< 2% if referred to a flat level of $5 \cdot 10^{-3}$ cts/cm^2/s/keV), however characteristic fluorescence lines are relatively pronounced and it might be desirable to avoid them. Coating the mesh with 5 μm Au produces complete suppression of the fluorescence lines from the bulk material, although two small Au L-fluorescence features appear at ~9.7 keV and ~11.4 keV (Fig. 10). Coating the mesh with 7 μm Ag produces as well complete suppression of the fluorescence lines from the bulk material, and no fluorescence features from the coating are present in the spectrum
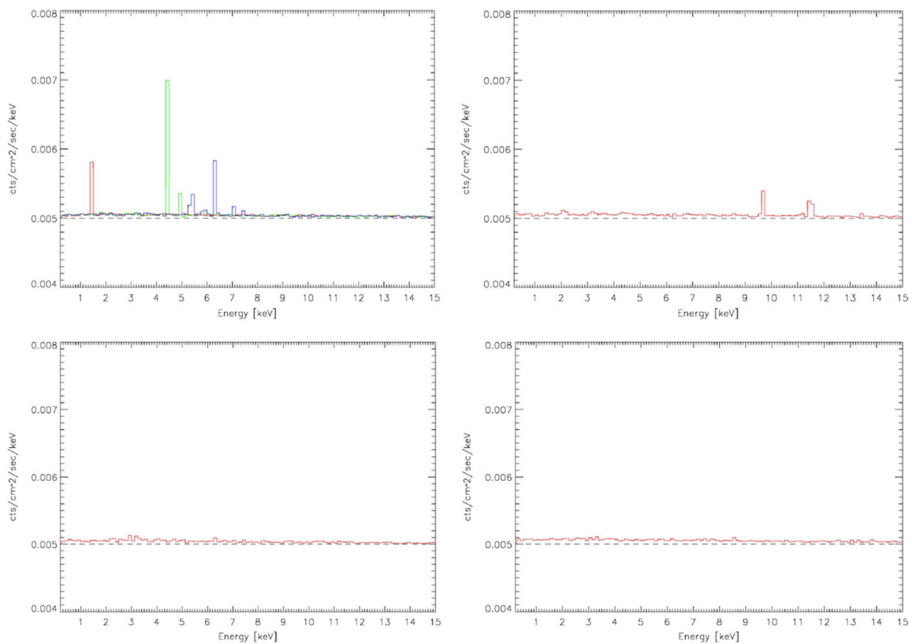
Fig. 10 *Top left*: overall NXB expected from a mesh in Al (*red curve*), Ti (*green curve*) and stainless steel (*blue curve*) mounted above the detector, assuming a flat baseline NXB $5\cdot10^{-3}$ cts/cm²/s/keV in absence of a mesh The excess continuum introduced by the mesh is $<10^{-4}$ cts/cm²/s/keV, however characteristic K_α lines are relatively pronounced. *Top right*: bulk fluorescences can be completely absorbed by coating the mesh with 5 μm Au, although two small L-fluorescence features appear in the spectrum. *Bottom left*: coating with 7 μm Ag also produces complete suppression of the bulk fluorescences without introducing other features. *Bottom right*: no spectral features are present in the NXB of a mesh in C-fibre

(Fig. 10), as the Ag L-yield is much smaller than that of Au. For a mesh in Ti 4 μm Ag is enough, for a mesh in Al 1 μm Ag is enough. As an alternative that could be worth some investigation, C-fibre is a lightweight, hard and very resistant material with a fluorescence yield much smaller than a metal, therefore no fluorescence features are present in the spectrum generated by a mesh in C-fibre (Fig. 10). Moreover, C-fibre offers an X-ray transmissivity significantly higher than a metal, thus it looks like an attractive candidate material to fulfill the request on the throughput at 6–7 keV. Since it seems unlikely to find on the market C-fibre wires/rods with the desired specifications to build a criss-cross mesh and C-fibre being not even suited for chemical etching, an alternative way would be to drill a thin C-fibre sheet to open on it an array of tiny cells. However, using conventional drilling techniques, e.g. exploiting diamond tips, a wall of material as thin as ~100 μm between cells would most likely fail during the cutting loads. To overcome these problems, cutting by laser could be preferred. As an example, we realized a small prototype mesh 2 × 2 cm with 5 mm pitch and 0.15 mm wire width cutting out a commercial 0.25 mm thick pre-impregnated C-fibre sheet with a fibre laser (Fig. 11). Using a higher quality C-fibre sheet and playing a bit with the laser parameters it may be possible to find a better compromise between laser power, laser frequency, scanner speed and focus point to improve the result and obtain a thinner width. Nevertheless, as truncated fibres may not be as strong as the integral ones the mechanical robustness of a mesh in C-fibre obtained by cutting a C-fibre sheet should

Fig. 11 A mini-mesh 2 × 2 cm with 5 mm pitch and 0.15 mm wire width manufactured at O. R. Lasertechnologies by cutting a commercial 0.25 mm thick pre-impregnated C-fibre sheet with a fibre laser

be carefully verified with specific tests (e.g. under vibration stress). Weaving a criss-cross mesh with Mylar thin wires seems another promising manner of manufacturing a high-throughput light mesh.

4 Soft protons and ions

In the discussion reported in Section 3 we did not consider the contribution to the NXB that may result from environmental soft protons and ions. As we mentioned, a 4 cm thick Al shield is able to stop, on average, protons up to ~110 MeV. Therefore, environmental soft (< 10 MeV) solar and/or trapped protons and ions in principle would not be an issue, however they may be funneled to the focal plane through the telescope. This effect has been experienced by both Chandra [8] and XMM (www.cosmos.esa.int/web/xmm-newton/background). Although the DEPFET detector developed for ATHENA is back-illuminated and likely less susceptible to radiation damage than a CCD, as no charge transfer is applied, soft protons and ions reaching the focal plane may at least contribute to increase the NXB level. As a matter of fact, quite a lot of XMM observations were strongly affected by soft protons. The concern is even bigger for ATHENA, due to its much larger collecting area. For this reason, a magnetic diverter is being investigated to reduce the possible flux of charged particles at the focal plane well below the threshold of $5 \cdot 10^{-3}$ cts/cm^2/s/keV. Two inputs would be helpful in this analysis: 1) the expected flux of charged particles that will be entering the telescope from the environment and 2) the response function of the ATHENA silicon pore optics (SPO), which would allow to calculate the effective area for soft protons and ions. While the first is largely uncertain due to the lack of radiation monitors around L2 in the softer energy range, there are theoretical models that describe the physics underlying the reflection of soft protons and ions at grazing angle incidence and predict the scattered distributions. However, work has still to be done to validate and possibly improve the models, as the few existing experimental data are not sufficient for a full comprehension

of the mechanism at work. A setup for tests of proton and ion scattering at grazing incidence off X-ray mirror samples has been constructed at the 3 MV proton and ion accelerator of the University of Tübingen in the past few years [9]. The current implementation allows for a sampling of the distribution of the scattered protons along the polar direction Θ, in a range of polar angles from ~0.1° to ~5° (with respect to the target surface), by means of a surface barrier silicon diode movable along the axis perpendicular to the incident proton beam, as shown in Fig. 12. Some measurements have already been performed using eROSITA mirror parts as a target [9]. In the framework of the AHEAD project we are planning verification of SPO samples as well. As it is expected that soft protons and ions also undergo scattering along the azimuthal direction Φ, future tests will be conducted with a modified detection system using three diodes in a row jointly movable along the vertical axis, one in the middle and two fixed at the sides: for each diode position along the polar direction, this configuration will allow to sample the scattered distribution in the azimuthal range of angles - 2° < Φ < + 2°. This should permit, in particular, a more meaningful comparison of the experimental data with the Remizovich two dimensional distribution [10].

5 Conclusion

We presented the status of the activities for the assessment of the NXB and optimization of the camera design for the ATHENA/WFI. Although the work is still in progress, some results appear already consolidated. A thin passivation deposited on the non-illuminated side of the detector is technically feasible and would effectively reduce the GCR NXB by ~30% at energies <7 keV. Nevertheless, in the current baseline shielding configuration the drawback is photon leakage, so that an about twice larger NXB than the requirement may be expected. This is because, due to the high transmissivity of the 4 cm thick Al shield to high energy CXB photons, they can penetrate through it and undergo Compton scattering in the relatively thick depleted volume, with production of low energy recoiling electrons, that behave like photoelectrons and contribute to the NXB. To suppress this component we are investigating some improved shielding configurations that exploit thin layers of both high-Z and low-Z materials, although
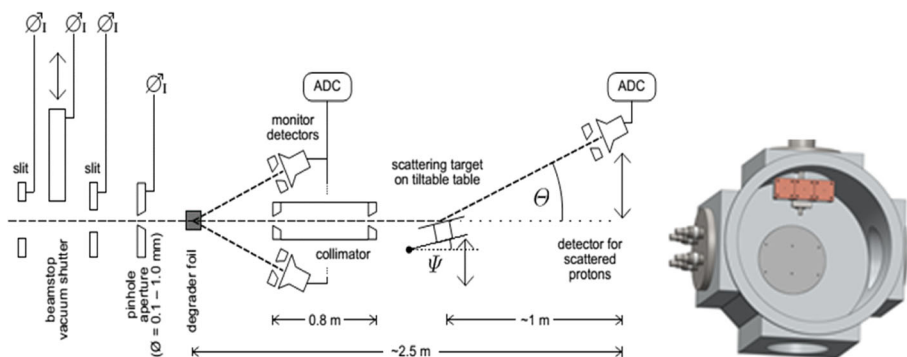

Fig. 12 *Left:* Schematic of the setup built at the 3 MV proton accelerator of the University of Tübingen for testing soft proton scattering at grazing incidence. *Right:* the detection system with three diodes on a row will enable scatter measurements along both the polar and azimuthal directions (image credits: S. Diebold)

in this case the production of secondary neutrons by spallation and activation effects should be carefully assessed. Such a multilayer shield should replace the low-Z internal layer planned to suppress the K-fluorescence from the Al proton shield and other sub-structures around the detector. However, as mentioned such a shield may be structured as a multilayer using high-Z and low-Z materials in order to optimize the trade off between NXB and NIEL. As another consolidated result, we verified that a mesh in metal, that most likely will be used to sustain the OBF, will not impact significantly the continuum NXB, however a coating should be applied as a countermeasure against possible fluorescences. The contribution to NXB from soft protons and ions scattered through the SPO optics is still an open question, for this scope a charged particle diverter is foreseen, that should allow to get rid of soft charged particle contamination at the focal plane. In this regard, we are planning to perform in the near future soft proton and ion scattering tests on SPO samples, which are expected to provide useful information for the characterization of the ATHENA effective area to charged particles and for the design of the magnetic diverter. Finally, we stress that the time distribution of the simulated NXB events has not been yet investigated and hence no method of NXB reduction based on discarding WFI frame patterns has been applied in the presented study, which may effectively help to refine and lower to some extent the ultimate NXB level.

References

1. Rau, A., et al.: The Hot and Energetic Universe: The Wide Field Imager (WFI) for Athena+, arXiv: 1308.6785 (2013)
2. Nandra, K., et al.: The Hot and Energetic Universe: a White Paper presenting the science theme motivating the Athena+ mission, arXiv:1306.2307 (2013)
3. Barret, D., et al.: The Hot and Energetic Universe: The X-ray Integral Field Unit (X-IFU) for Athena+, arXiv:1308.6784 (2013)
4. Tenzer, C., et al.: Monte-Carlo background simulations of present and future detectors in X-ray astronomy. Proc. of SPIE. **7011**, 7011–702G (2008)
5. Gruber, D.E., et al.: The Spectrum of diffuse cosmic hard X-rays measured with HEAO 1. APJ. **520**, 124 (1999)
6. Perinati, E., et al.: The radiation environment in L-2 orbit: implications on the non-X-ray background of the eROSITA pn-CCD cameras. Exp. Astr. **33**, 39 (2012)
7. Barbera, M., et al.: The optical blocking filter for the ATHENA wide field Imager: ongoing activities towards the conceptual design. Proc. of SPIE. **9601**, 9601–9609 (2015)
8. Prigozhin, G.Y., et al.: Characterization of radiation damage in Chandra X-ray CCDs. Proc. of SPIE. **4140**, 123 (2000)
9. Diebold, S., et al.: Soft proton scattering efficiency measurements on x-ray mirror shells. Exp. Astr. **39**, 343 (2015)
10. Remizovich, V.S., et al.: Small-angle multiple scattering of light particles at glancing incidence for screened coulomb interaction. Sov. Phys. JETP. **52**, 2 (1980)